Volume 54
Number 37
7 October 2025
Pages 13793-14228

Dalton Transactions

An international journal of inorganic chemistry

rsc.li/dalton

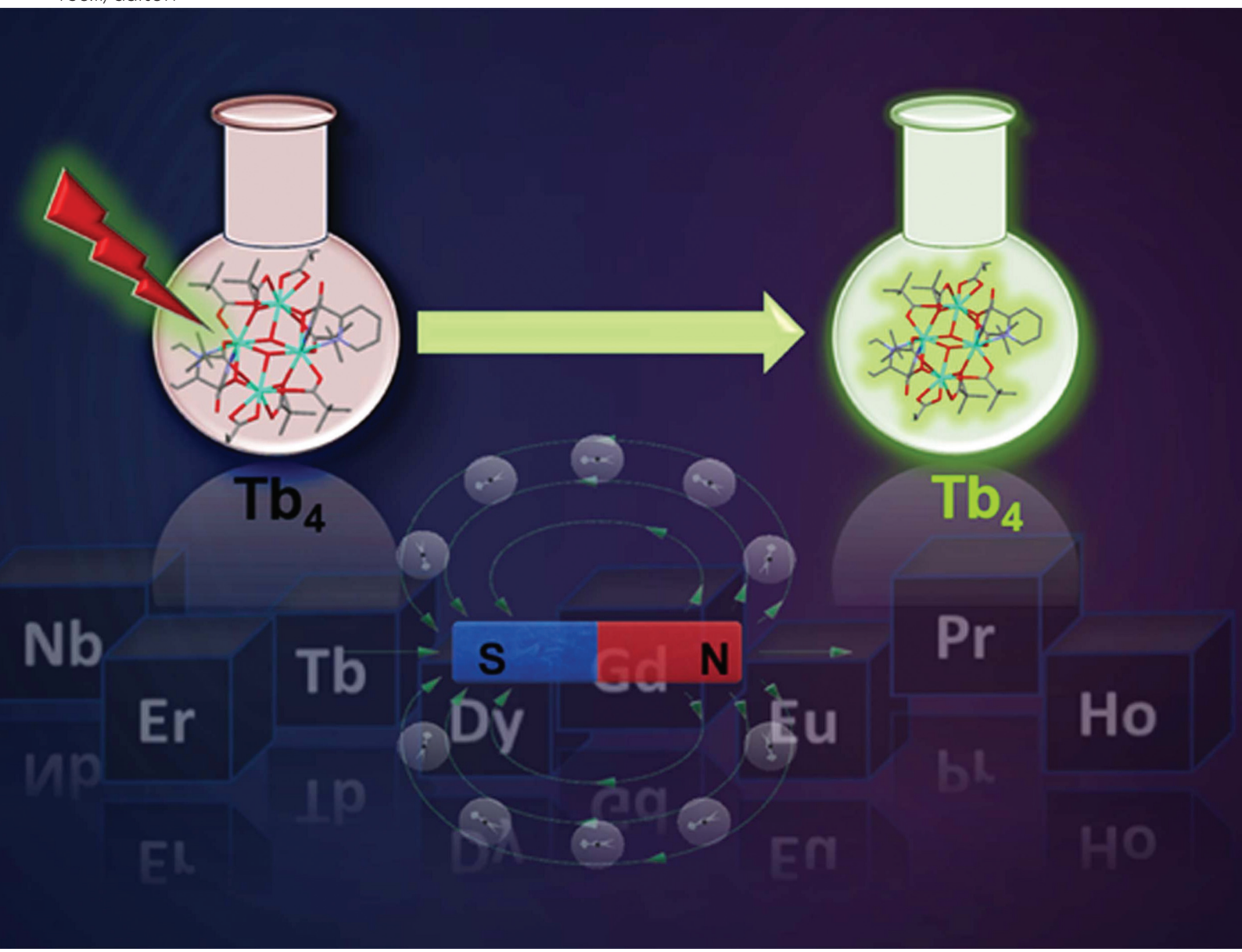

ISSN 1477-9226

ROYAL SOCIETY OF CHEMISTRY

PAPER

Björn Schwarz, Saurabh Kumar Singh, Joydeb Goura *et al.*
Tetranuclear $\{Ln^{III}\}_4$ complexes possessing homometallic *O-capped* structural subunits: study of magnetic and photoluminescent properties

Dalton Transactions

ROYAL SOCIETY OF CHEMISTRY

PAPER

View Article Online
View Journal | View Issue

Cite this: *Dalton Trans.*, 2025, **54**, 13879

Tetranuclear $\{Ln^{III}\}_4$ complexes possessing homometallic *O-capped* structural subunits: study of magnetic and photoluminescent properties

Purbashree Halder,[a] Nandini Barman,[a] Ibtesham Tarannum,[c] Subrata Mukhopadhyay,[a] Björn Schwarz,*[b] Saurabh Kumar Singh*[c] and Joydeb Goura*[a,d,e]

Received 24th October 2024,
Accepted 6th August 2025

DOI: 10.1039/d4dt02976c

rsc.li/dalton

A series of homometallic tetranuclear Ln_4 complexes, $[Ln_4(\mu_3\text{-}OH)_2\{py_2C(OH)O\}_2(O_2CCMe_3)_8]$ [$\{py_2C(OH)O\}^-$ = monoanionic *gem*-diol form of di-2-pyridyl ketone; Ln = Nd (**1**), Eu (**2**), Tb (**3**), Dy (**4**), Er (**5**) and Yb (**6**)], have been synthesized and characterized. The asymmetric unit of each of the tetranuclear derivatives comprises the dinuclear motif, $[Ln_2(\mu_3\text{-}OH)\{py_2C(OH)O\}(O_2CCMe_3)_4]$. The core structure of this Ln_4 family possesses two homometallic *O-capped* structural subunits, Ln^{III}_3O, which are further connected through the bridging μ_3-OH ligands. Mean plane analysis indicates that all the lanthanide centers lie in the same plane. There are two types of eight-coordinated lanthanide centers present. The shape analysis revealed that the Ln1 center possesses a distorted elongated trigonal bipyramidal geometry while the Ln2 center has a distorted Johnson elongated triangular bipyramidal geometry. Solid-state room temperature photoluminescence studies of **1–5** show the ligand center emission band at 306 nm when excited at 270 nm. Compound **1**, when excited at 380 nm emits at 517, 624, and 724 nm. On the other hand, excitation at 360 nm of compound **3**, leads to emission peaks at 489, 542, 583, 590, and 624 nm. These bands are due to the f–f transitions of the Tb(III) centers. For all complexes, the dependence of direct current (DC) and alternating current (AC) magnetization on temperature and magnetic field was measured. The magnetic anisotropy and magnetic relaxation mechanism were also studied using the complete active space self-consistent field (CASSCF) methodology for complexes **1–6**. The SINGLE_ANISO module is used to extract the relevant spin-Hamiltonian parameters. We have calculated the magnetic exchange couplings (J_1–J_3) for all the complexes. For complexes **3** and **4**, we observed a sizable tunnel splitting of 1.5×10^{-3} cm^{-1} and 1.9×10^{-3} cm^{-1}, indicating that QTM is still a dominant mechanism for magnetic relaxation in the exchange-coupled systems, resulting in diminished SMM behaviour.

Introduction

Multi-dentate coordinating organic and inorganic ligands have been extensively used for developing lanthanide ion-based single-molecule magnets (SMMs).[1] Among them, the di-2-pyridyl ketone, $(py)_2CO$, has ubiquitous coordination capabilities, since it contains hetero-donor sites including one oxygen and two nitrogen atoms. The neutral $(py)_2CO$ can act as a bidentate chelating ligand, while tri- or tetra-dentate behavior has been observed for the geminal diol, which is formed in the presence of a base. The $(py)_2CO$ ligand has strong coordination binding capability towards soft and hard metal ions. In addition, two pyridine groups attached to the carbonyl slightly enhance the electrophilic nature of the carbonyl group. As a result, formation of the hemiketal is faster in the presence of solvents (such as H_2O, MeOH, EtOH, *etc.*) (Chart 1).[2] The hemiketal ligand has beneficial properties for binding with oxophilic lanthanide ions. On the other hand, the hydrazine derivative of the $(py)_2CO$ ligand shows strong fluorescence properties in an acidic medium.[3]

Therefore, the neutral $(py)_2CO$ has the potential ability to assemble polynuclear lanthanide complexes. Polymetallic

[a]*Department of Chemistry, Jadavpur University, Kolkata-700032, India. E-mail: jgoura@chemistry.du.ac.in, joydebgoura@gmail.com*
[b]*Karlsruhe Institute of Technology (KIT) – Institute for Applied Materials (IAM), Hermann-von-Helmholtz-Platz 1, 76344 Eggenstein-Leopoldshafen, Germany. E-mail: bjoern.schwarz@kit.edu*
[c]*Computational Inorganic Chemistry Group, Department of Chemistry, Indian Institute of Technology Hyderabad, Kandi, Sangareddy, Telangana-502284, India. E-mail: sksingh@chy.iith.ac.in*
[d]*Department of Chemistry, University of Delhi, Delhi-110007, India*
[e]*Department of Chemistry, Bangabasi College, Kolkata-700009, West Bengal, India*

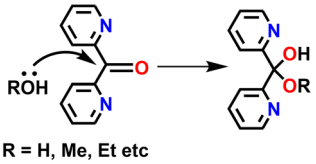

Chart 1 Hemiketal form of di-2-pyridyl ketone.

lanthanide complexes have generated great interest over the last few decades owing to their potential applications in modern molecular qubits,[4] molecular spintronics,[5] quantum computations,[6] magnetic refrigeration,[7] photochromic materials,[8] and particularly in single-molecule magnets (SMMs).[1] SMM properties have been extensively studied for polynuclear lanthanide complexes due to their high ground spin state (S) and Tb(III),[9] Dy(III),[10] Ho(III),[11] and Er(III)[12] ions show strong magnetic anisotropy (D). However, achieving a high spin ground state by ferromagnetic coupling between the lanthanide ions is very challenging. Simultaneously, the blocking temperature is another key factor in controlling SMM behavior that is certainly determined by the magnetic anisotropy, caused by zero-field splitting (ZFS).[13] A purely uniaxial negative ZFS parameter D is desirable for good SMM characteristics with slow magnetic spin–lattice relaxation and long conservation of the magnetic Ising limit.[13] The high uniaxial anisotropy possesses a large energy barrier, U_{eff}, with accompanying high blocking temperature for reversal of magnetization.[14]

An effective energy barrier that ensures slow spin–lattice relaxation strongly depends on the coordination environment and the geometry around the Ln(III) ion.[15] The electronic and steric factors of the ligands play crucial roles in determining the geometry and control of the magnetic properties. A survey of the literature revealed that varieties of polynuclear lanthanide complexes have been reported such as those with di-, tri-, tetra-, penta-, hexa-, and higher nuclearities.[16] Among them, tetranuclear derivatives have received significant attention owing to their structural arrangements [*e.g.* rhomboid, cubane, butterfly, square, rectangle, chain-like, linear, Y, see-saw, irregular zigzag, square grids (2 × 2), *etc.*] and magnetic behavior depending on the organic ligand backbone.[16] So, appropriate designs of the organic ligands can regulate the structural patterns and coordination numbers that can modulate the coordination geometry and magnetic properties. Various tetranuclear lanthanide derivatives have been reported based on several organic and inorganic ligands.[16] Indeed, the neutral $(py)_2CO$ as primary ligand-based tetranuclear lanthanide complexes have not been reported yet.

In this regard, the $(py)_2CO$ ligand is of great interest for assembling tetranuclear lanthanide complexes due to its multi-dentate nature and control of magnetic and photoluminescent properties. Accordingly, herein, we report a series of tetranuclear homometallic *O-capped* lanthanide complexes **1–6** based on the $(py)_2CO$ ligand. Detailed magnetic and luminescence studies have been conducted.

Experimental

Reagents and general procedures

Solvents and other general reagents used in this work were purified according to standard procedures.[17] Di-2-pyridyl ketone [$(py)_2CO$] and sodium pivalate hydrate (NaPiv) were acquired from TCI (Tokyo, Japan). NEt_3 was obtained from S.D. Fine-Chem Ltd. $NdCl_3{\cdot}6H_2O$, $EuCl_3{\cdot}6H_2O$, $ErCl_3{\cdot}6H_2O$, and $YbCl_3{\cdot}6H_2O$ were bought from Alfa Aesar, while $TbCl_3{\cdot}6H_2O$ was obtained from SRL and $DyCl_3{\cdot}6H_2O$ from Sigma-Aldrich, and were used as received.

Instrumentation

Melting points were measured using a JSGW melting point apparatus and the presented values are uncorrected. Fourier transform infrared (FT-IR) spectra were recorded with a PerkinElmer LX-1 FT-IR spectrophotometer (4000–400 cm^{-1}) by using a modern diamond attenuated total reflectance (ATR) accessory. Elemental analyses of the compounds were performed using a PerkinElmer 2400 Series-II CHN analyzer. The solid-state emission spectra were recorded on a PerkinElmer Lambda 20 spectrophotometer.

X-ray crystallography

Single-crystal X-ray structural studies of **1–6** were performed on a Bruker SMART APEX CCD diffractometer. Data were collected using a graphite-monochromated MoK_α radiation source (λ = 0.71073 Å). The crystals did not degrade/decompose during data collection. Data collection, and structural solutions and refinements were performed using the SMART, SAINT and SHELXTL programs, respectively.[18a–f] All of the non-hydrogen atoms were refined anisotropically using full-matrix least-square procedures. All of the hydrogen atoms were fixed at idealized positions, and a riding model was used. All of the mean plane analyses and molecular drawings were obtained using Diamond (version 3.1).

DC and AC magnetometry

Direct current (DC) and alternating current (AC) magnetometry was conducted using a Physical Property Measurement System (PPMS) DynaCool from Quantum Design equipped with an ACMS-II option. Powdered complexes of **1** (Nd), **2** (Eu), **3** (Tb), **4** (Dy), **5** (Er), and **6** (Yb) were used when measuring their DC magnetometry values. The sample powders were filled into gelatin capsules (QDC-AGC1 from Quantum Design) and mechanically fixed with Icosane (about 50 mg) to prevent particle reorientation. The capsules were fixed with some polyimide tape within magnetically neutral sample holder straws (QDS-8000-001 from Quantum Design) and attached to the sample holder rod. DC magnetization *vs.* temperature was measured at a magnetic field of 1000 Oe from 2 K to 50 K in settle mode and from 51 K to 200 K in sweep mode at a 1 K min^{-1} heating rate. The temperature step size for signal acquisition was 1 K with a signal averaging time of 10 seconds. Magnetization *vs.* magnetic field was measured at 2, 5, 10, 15, 20, 25, 35, 50, and 300 K up to 7 T (complexes **3** and **4** were not measured at 300 K) with a signal averaging time of 10 seconds

and a three-fold redundancy per measuring point. Due to the strong magnetic signal stemming from the lanthanoids, no corrections for diamagnetic contributions have been made. AC susceptibility was measured from 50 Hz to 10 kHz at 27 different frequencies with a log-distribution at 2 K at various magnetic DC fields, as indicated in the corresponding figures (maximum field was 2500 Oe). The AC excitation field was 5 Oe with an average time per measuring point of 10 seconds.

Synthesis

General procedure for the synthesis of complexes 1–6. The following general protocol was utilized for the synthesis of homometallic tetranuclear lanthanide complexes. $LnCl_3{\cdot}6H_2O$ was added to a stirred solution of di-2-pyridyl ketone $(py)_2CO$ in methanol (20 mL). To this solution, sodium pivalate (NaPiv) hydrate and triethylamine (NEt_3) were added. The mixture was stirred for 30 minutes at 60 °C, affording a clear colorless solution. This solution was evaporated in a rotary evaporator to dryness, the product re-dissolved in methanol, and then filtered. The filtrate was allowed to evaporate slowly at room temperature. After two weeks, colorless crystals suitable for X-ray diffraction had been formed. Specific quantities of the reactants involved in each reaction, yields of the products, and their characterization data are given below.

$[Nd_4(\mu_3\text{-}OH)_2\{py_2C(OH)O\}_2(O_2CCMe_3)_8]$ (1). Quantities: $(py)_2CO$ (0.062 g, 0.336 mmol), $NdCl_3{\cdot}6H_2O$ (0.060 g, 0.168 mmol), NEt_3 (0.4 mL, 2.869 mmol), NaPiv (0.072 g, 0.507 mmol). Yield: 0.046 g, 53% (based on Nd). Mp: 200 °C (d). IR (KBr) (cm^{-1}): 3362(br), 2961(br), 1514(w), 1482(s), 1415(s), 1374(w), 1226(m), 1147(m), 1088(m), 1064(s), 1043(w), 1011(m), 938(w), 896(m), 846(m), 812(s), 790(m), 758(s), 631(m), 593(s), 593(m), 400(s). Anal. calcd for $C_{62}H_{92}N_4Nd_4O_{22}$ (1822.39): C, 40.86; H, 5.09; N, 3.07. Found: C, 39.61; H, 4.88; N, 2.93.

$[Eu_4(\mu_3\text{-}OH)_2\{py_2C(OH)O\}_2(O_2CCMe_3)_8]$ (2). Quantities: $(py)_2CO$ (0.061 g, 0.336 mmol), $EuCl_3{\cdot}5H_2O$ (0.062 g, 0.168 mmol), NEt_3 (0.4 mL, 2.869 mmol), NaPiv (0.072 g, 0.507 mmol). Yield: 0.041 g, 50% (based on Eu). Mp: 200 °C (d). IR (KBr) (cm^{-1}) 2963(br), 1579(w), 1521(w), 1485(s), 1425(s), 1378(w), 1362(s), 1227(m), 1166(m), 1038(m), 1014(w), 943(w), 898(m), 807(m), 759(s), 671(s), 631(m), 596(s), 403(s). Anal. calcd for $C_{62}H_{92}Eu_4N_4O_{22}$ (1853.28): C, 40.18; H, 5.00; N, 3.02. Found: C, 39.92; H, 4.81; N, 2.86.

$[Tb_4(\mu_3\text{-}OH)_2\{py_2C(OH)O\}_2(O_2CCMe_3)_8]$ (3). Quantities: $(py)_2CO$ (0.062 g, 0.336 mmol), $TbCl_3{\cdot}5H_2O$ (0.063 g, 0.168 mmol), NEt_3 (0.4 mL, 2.869 mmol), NaPiv (0.072 g, 0.507 mmol). Yield: 0.040 g, 51% (based on Tb). Mp: 200 °C (d). IR (KBr) (cm^{-1}): 2961(br), 1567(w), 1516(w), 1485(s), 1424(s), 1377(w), 1297(w), 1227(m), 1209(m), 1117(m), 1164(s), 1079(m), 1079(m), 1039(w), 943(w), 896(m), 817(m), 808(m), 791(m), 759(s), 670(s), 649(m), 632(m), 595(s), 564(m), 400(s). Anal. calcd for $C_{62}H_{92}Tb_4N_4O_{22}$ (1881.13): C, 39.59; H, 4.93; N, 2.98. Found: C, 39.32; H, 4.74; N, 2.83.

$[Dy_4(\mu_3\text{-}OH)_2\{py_2C(OH)O\}_2(O_2CCMe_3)_8]$ (4). Quantities: $(py)_2CO$ (0.062 g, 0.336 mmol), $DyCl_3{\cdot}5H_2O$ (0.064 g, 0.168 mmol), NEt_3 (0.4 mL, 2.869 mmol), NaPiv (0.072 g, 0.507 mmol). Yield: 0.042 g, 52% (based on Dy). Mp: 200 °C (d). IR (KBr) (cm^{-1}): 2981(br), 1577(w), 1517(w), 1485(s), 1424(s), 1377(w), 1297(w), 1227(m), 1210(m), 1114(m), 1137(s), 1079(m), 1014(w), 943(w), 826(m), 816(m), 791(m), 758(s), 670(s), 658(w), 649(m), 632(m), 596(s), 565(m), 532(m), 400(s). Anal. calcd for $C_{62}H_{92}Dy_4N_4O_{22}$ (1895.42): C, 39.29; H, 4.89; N, 2.96. Found: C, 39.04; H, 4.69; N, 2.82.

$[Er_4(\mu_3\text{-}OH)_2\{py_2C(OH)O\}_2(O_2CCMe_3)_8]$ (5). Quantities: $(py)_2CO$ (0.062 g, 0.336 mmol), $ErCl_3{\cdot}5H_2O$ (0.065 g, 0.168 mmol), NEt_3 (0.4 mL, 2.869 mmol), NaPiv (0.072 g, 0.507 mmol). Yield: 0.040 g, 50% (based on Er). Mp: 200 °C (d). IR (KBr) (cm^{-1}): 2961(br), 1579(w), 1519(w), 1460(s), 1426(s), 1378(w), 1297(w), 1228(m), 1212(m), 1167(m), 1150(m), 1080(s), 1037(w), 944(w), 898(m), 809(m), 791(m), 671(s), 650(w), 650(m), 632(m), 598(s), 567(m), 534(m), 400(s). Anal. calcd for $C_{62}H_{92}Er_4N_4O_{22}$ (1914.46): C, 38.90; H, 4.84; N, 2.93. Found: C, 38.66; H, 4.62; N, 2.79.

$[Yb_4(\mu_3\text{-}OH)_2\{py_2C(OH)O\}_2(O_2CCMe_3)_8]$ (6). Quantities: $(py)_2CO$ (0.062 g, 0.33 mmol), $YbCl_3{\cdot}5H_2O$ (0.066 g, 0.168 mmol), NEt_3 (0.4 mL, 2.869 mmol), NaPiv (0.072 g, 0.507 mmol). Yield: 0.040 g, 50% (based on Er). Mp: 200 °C (d). IR (KBr) (cm^{-1}): 2961(br), 1579(w), 1519(w), 1460(s), 1426(s), 1378(w), 1297(w), 1228(m), 1212(m), 1167(m), 1150(m), 1080(s), 1037(w), 944(w), 898(m), 809(m), 791(m), 671(s), 650(w), 650(m), 632(m), 598(s), 567(m), 534(m), 400(s). Anal. calcd for $C_{62}H_{92}Yb_4N_4O_{22}$ (1937.64): C, 38.43; H, 4.79; N, 2.89. Found: C, 38.19; H, 4.58; N, 2.77.

Results and discussion

Synthesis

The utility of di-2-pyridyl ketone, $(py)_2CO$, as a ligand has been pioneered, among others, by Spyros P. Perlepes and his research group.[2,19] Most of this work pertains to compounds that possess 3d- or 3d/4f-based magnetic clusters.[2,19] The interesting phenomenon of the $(py)_2CO$ ligand is that the coordination binding modes can be fine-tuned depending on the reaction medium (*i.e.* neutral or germinal diol systems) (*vide supra*) (Chart 1).[2,19] The multi-dentate nature of $(py)_2CO$ provides the potential for assembling tetranuclear lanthanide magnetic ensembles. In addition, the NaPiv ligand plays a cluster-expanding role for the formation of the tetranuclear lanthanide complexes. Therefore, in the reaction of lanthanide salts with $(py)_2CO$ and NaPiv in the presence of NEt_3 as a base, a series of tetranuclear homometallic lanthanide complexes **1–6**, with general formula $[Ln_4(\mu_3\text{-}OH)_2\{py_2C(OH)O\}_2(O_2CCMe_3)_8]$ (Scheme 1), are afforded. Compounds **1–6** have been characterized by various physicochemical methods, such as IR, X-ray single-crystal, magnetic, and luminescence studies. The IR spectra of compounds **1–6** exhibit a medium intensity band at 2961 cm^{-1}, which is assigned to the ν(OH) stretching vibration of the $[(py)_2C(OH)O]^-$ ligand. The spectra also show bands at 1577 cm^{-1} due to the formation of the metal complex *via* the *in situ* generated germinal diol of the $(py)_2CO$ ligand[20] [free carbonyl stretching vibration band of $(py)_2CO$ is ν(C=O), at 1684 cm^{-1}].[20] The bands at 1037 cm^{-1},

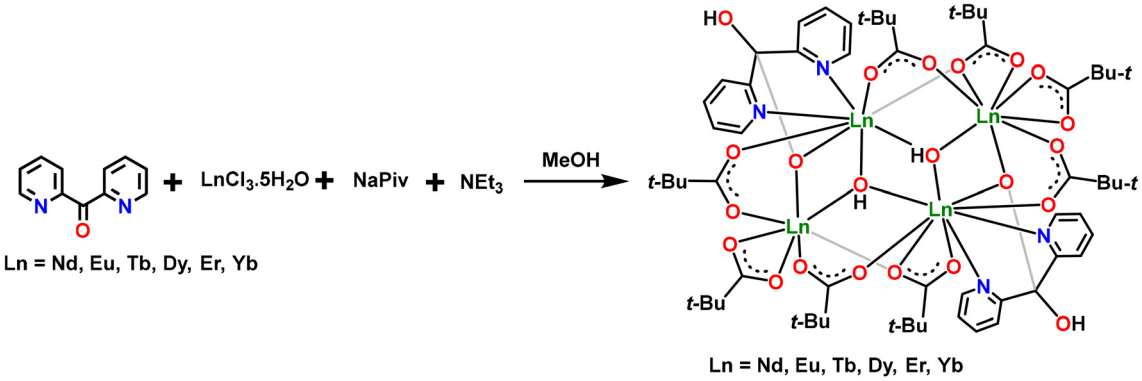

Scheme 1 Synthesis of tetranuclear Ln^{III}_4 complexes **1–6**.

758 cm^{-1}, and 594 cm^{-1} are attributed to out-of-plane bending and stretching vibrations of pyridyl C–H bonds, and in-plane pyridyl ring deformation vibration, respectively.[20]

Molecular structures of 1–6

The molecular structures of all the complexes **1–6** were determined by single-crystal X-ray diffraction. The crystallographic parameters of **1–6** are given in Tables S1 and S2. X-ray crystallographic analysis has revealed that complexes **1–6** are isomorphic. All the isostructural complexes crystallize in the monoclinic system with the *C*2/*c* (*Z* = 4) space group. The asymmetric unit of all the compounds contains half of the total molecule, $[Ln_2(\mu_3\text{-OH})\{py_2C(OH)O\}(O_2CCMe_3)_4]$, and a representative example is shown in Chart 2 and Fig. 1. In view of their structural similarity, only compound **4** will be described in the main manuscript, while details of the parameters of the remaining structures are given in the SI (Fig. S1–S5).

The molecular structure of **4** is given in Scheme 1 and Fig. 2. The tetranuclear homometallic lanthanide complex is built through the multiple coordination action of two $[\{py_2C(OH)O\}]^-$, two μ_3-OH, and eight bridging pivalate ligands. The coordination modes observed for all the ligands are displayed in Chart 3. Each $[\{py_2C(OH)O\}]^-$ ligand holds two Dy(III) ions *via* chelating and bridging coordination modes of the monoanionic *gem*-diol ($\eta^1{:}\eta^2{:}\eta^1{:}\mu_2$), and the Dy–O bond distances are Dy(1)–O(1), 2.289(2) Å and Dy(2)–O(1), 2.275(2) Å (Fig. 2 and Scheme 1). The two nitrogen centers of the $[\{py_2C(OH)O\}]^-$ ligand exclusively bind in a $\eta^1{:}\eta^1$ fashion to the Dy1 center.

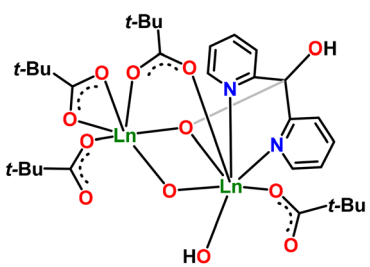

Chart 2 Asymmetric unit of complexes **1–6**.

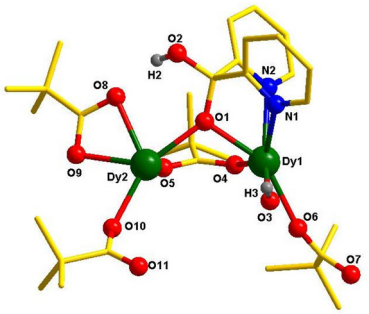

Fig. 1 The asymmetric unit of complex **4**. All hydrogen atoms have been omitted for clarity.

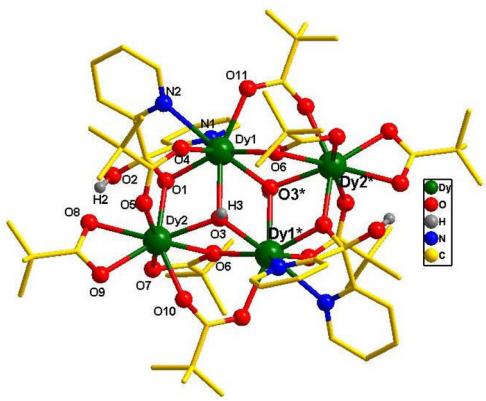

Fig. 2 Molecular structure of complex **4**. All hydrogen atoms have been omitted for clarity. Symmetry codes: Dy2* (1 − *x*, 1 − *y*, 1 − *z*), O3* (1 − *x*, 1 − *y*, 1 − *z*).

The Dy–N bond distances are Dy(1)–N(2), 2.537(2) Å and Dy(1)–N(1), 2.584(3) Å, and the corresponding bite angle <N(2)–Dy(1)–N(1) is 69.58(8)°. In addition, there are three types of binding coordination modes of pivalate ligands (Chart 3), where two of them act in a chelate fashion while the remaining six are bridged between the two Dy(III) centers. Finally, the four Dy(III) ions are held together by μ_3-OH bridging ligands, and the corresponding Dy–O bond distances are Dy1–O3, 2.335(2)

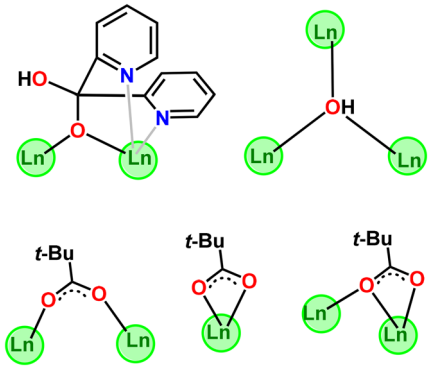

Chart 3 The coordination modes of all of the ligands as observed in the present study.

Å; Dy1*–O3, 2.413(2) Å; and Dy2–O31, 2.360(2) Å. The core structure consists of two incomplete cubic sub-units that can be designated as *O-capped* clusters (two Dy_3O_4 units) (Fig. 3). Similar types of structural motifs have been observed in main-group, 3d, 3d/4f, and 4f chemistry.[21]

There are two types of Dy(III) centers present and both are octa-coordinated. The coordination environment of Dy(1) and Dy(1)* centers are O_6N_2 while the Dy(2) and Dy(2)* centers are O_8. Systematic shape analysis of compound **4**, using SHAPE 2.1,[22] indicates that the Dy(1) possesses a distorted elongated trigonal bipyramidal geometry (Fig. 4a), while the Dy(2) centers hold a distorted Johnson elongated triangular bipyramidal geometry (Fig. 4b), respectively. The full shape analysis results can be found in the SI (Table S3). A mean plane analysis of the core of complex **4** reveals that all four Dy(III) centers are co-planar and present in the same plane (Fig. 5). Interestingly, out of two bridging μ_3-OH ligands, one lies above the plane while the other one lies below the plane and caps the three Dy(III) centers (Fig. 5). The distance between Dy(1) and Dy(2) is 3.696(7) Å, and that between Dy(2) and Dy(1)* is 3.838(9) Å, respectively. Additionally, all the compounds possess a non-coordinated free OH group from the *gem*-diol form of the $(py)_2CO$ ligand, which generates strong intramolecular hydrogen bonding with the coordinated pivalate ligand chelated to the Dy2 center (H-bond between O2–H2⋯O8 atoms) (Fig. 6 and Table S4). The H-bond distances

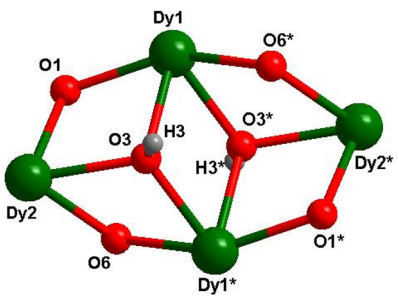

Fig. 3 The *O-capped* core structure of complex **4**. Symmetry codes: Dy2* (1 – *x*, 1 – *y*, 1 – *z*), O3* (1 – *x*, 1 – *y*, 1 – *z*).

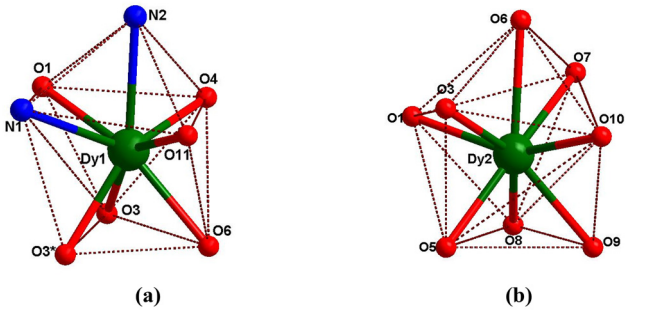

Fig. 4 The coordination geometry around the dysprosium centers of complex **4** is (a) distorted elongated trigonal bipyramidal and (b) distorted Johnson elongated triangular bipyramidal.

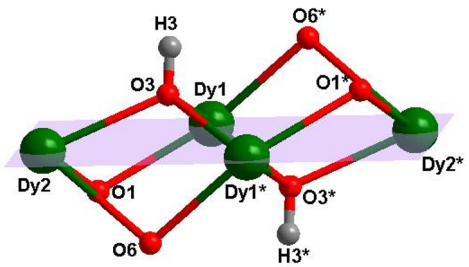

Fig. 5 The mean plane through all four Dy(III) ions in complex **4**.

O2–H2⋯O8 are 1.981(7) Å for **1**, 1.933(4) Å for **2**, 1.925(5) Å for **3**, 1.917(3) Å for **4**, 1.894(5) Å for **5** and 1.923(3) Å for **6** (Fig. S6), respectively. The H-bond distances decrease from compound **1** to **6** due to lanthanide contraction (Fig. S6 and Table S4). As the size of the lanthanide ions decreases, the corresponding H-bond distance values reduce.

Luminescence properties

The UV-vis spectrum of compound **4** was recorded in a methanol solution (Fig. S7). The absorption peak at 270 nm is assigned to the π–π* transitions of the $(py)_2CO$ ligand.

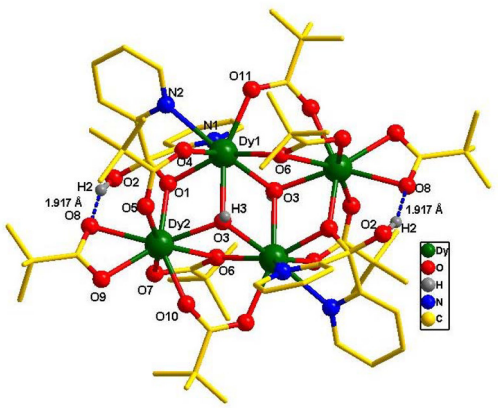

Fig. 6 Intramolecular hydrogen bonding of complex **4**.

The photoluminescence studies of complexes **1–5** were conducted at room temperature in the solid state. When excited at 270 nm in the solid state at room temperature, all the complexes show a bright intense emission peak at ~306 nm (Fig. 7a), which originates from ligand-centred transitions. Indeed, for **3**, an additional intense sharp band at 490 nm is observed, due to the f–f microstate transition $^5D_4 \rightarrow {}^7F_6$ of the Tb^{3+} ion (Fig. 7b).[23]

Exciting complex **1** at 380 nm, in the solid state at room temperature, causes emission signals at 517, 624, and 724 nm. The peaks at 517, 624, and 724 nm are ascribed to the $^4I_{9/2} \rightarrow {}^4G_{7/2}$, $^4I_{9/2} \rightarrow {}^2H_{11/2}$ and $^4I_{9/2} \rightarrow {}^4F_{7/2} + {}^4S_{3/2}$ transitions, respectively (Fig. S8).[24]

For **2**, emission peaks at 394, 562, 592, 613, and 630 nm are observed, when excited at 330 nm. As mentioned above, the intense emission peak at 394 nm stems from the O–Eu transition and reveals that the fluorescence of the $(py)_2CO$ ligand is more dominant than that of the Eu^{3+} ion.[25] Other emission peaks are assigned to the $^5D_0 \rightarrow {}^7F_0$, $^5D_0 \rightarrow {}^7F_1$, $^5D_0 \rightarrow {}^7F_2$, and $^5D_0 \rightarrow {}^7F_3$ transitions (Fig. S9).[26] The very weak band formally denotes the Laporte forbidden $^5D_0 \rightarrow {}^7F_0$ transition. On the other hand, signal intensity was enhanced for the magnetic dipole $^5D_0 \rightarrow {}^7F_2$ and forced electric dipole $^5D_0 \rightarrow {}^7F_2$ transitions, which suggested reduced symmetry of the europium coordination environment, where both are eight-fold coordinated and consistent with the results of crystallography and shape studies.[26]

Complex **3**, when excited at 360 nm, shows a blue emission peak at 493 nm caused by the $^5D_4 \rightarrow {}^7F_6$ transition. An intense green emission at 548 nm, yellow emission at 586 nm, and red emission at 622 nm are ascribed to the $^5D_4 \rightarrow {}^7F_5$, $^5D_4 \rightarrow {}^7F_4$, and $^5D_4 \rightarrow {}^7F_3$ transitions, respectively (Fig. 8).[23] The assigned peaks are in good agreement with luminescent Tb^{3+}complexes reported previously.[23]

Exciting complex **4** at 310 nm in the solid state at room temperature leads to luminescence peaks at 560 nm and 591 nm. The peaks at 560 nm and 591 nm are assigned respectively to the $^4F_{9/2} \rightarrow {}^6H_{13/2}$ and $^4F_{9/2} \rightarrow {}^6H_{11/2}$ transitions responsible for the Dy^{3+} center emission (Fig. S10).[23,27]

It is important to compare existing lanthanide complexes based on the neutral $(py)_2CO$ or deprotonated form of the *gem*-diol $[\{(py)_2(OH)CO\}^-$ or $\{(py)_2CO_2\}^-]$ ligand or its hemiacetal form $[\{(py)_2(OR)CO\}^-$; R = Me, Et] that have been reported with the current work. The literature survey revealed that few lanthanide complexes based on $(py)_2CO$ and its different ligand forms (*vide supra*) are known. It was observed that all reported lanthanide complexes are either mono- or di-nuclear derivatives (see Table S5) and assembled *via* the formation of monoanionic *gem*-diol $[\{(py)_2(OH)CO\}^-]$ or hemiacetal $[\{(py)_2(OR)CO\}^-$; R = Me, Et] ligands. To the best of our knowledge, no such lanthanide complexes utilizing neutral $(py)_2CO$ or di-deprotonated $[\{(py)_2CO_2\}^-]$ ligands have been reported. The first luminescent, mono- and di-nuclear Er(III) complexes, $[Er(NCS)_3\{(py)_2C(OR)(OH)\}_3]$ and $[Er_2(NCS)_3\{(py)_2C(OMe)O\}_3(MeOH)]$, were reported in 2006.[28] These complexes are derived from the hemiacetal forms $\{(py)_2(OEt)COH\}$ and

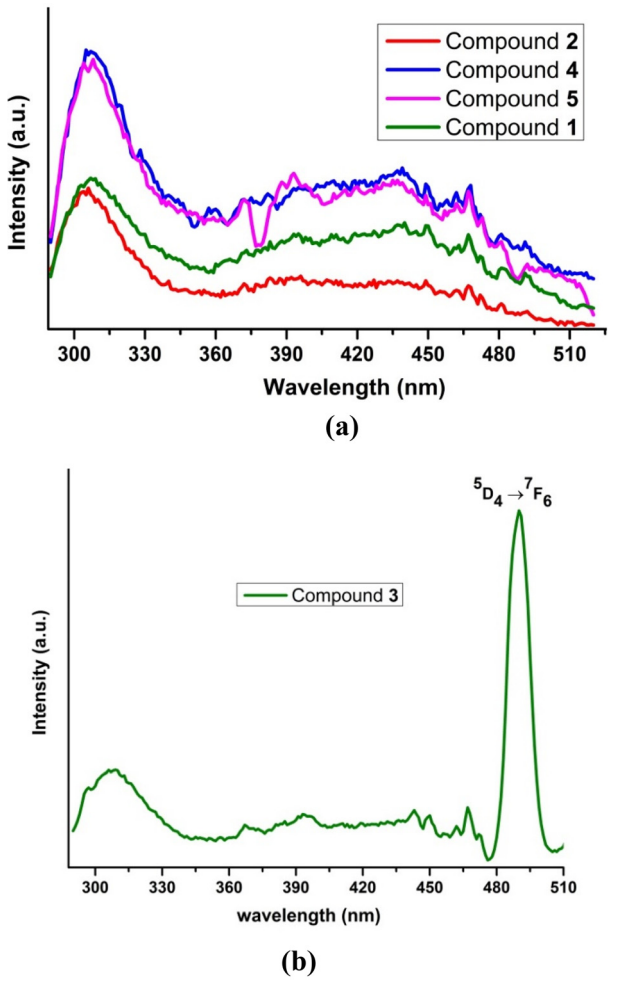

Fig. 7 The luminescence emission spectra of the complexes: (a) for **1** and **2** and **4** and **5**, and (b) for **3**, all in the solid state at room temperature upon excitation at 270 nm.

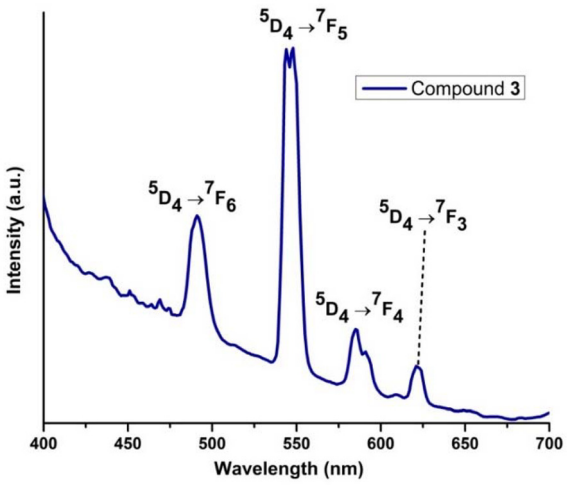

Fig. 8 Room-temperature solid-state emission spectrum for complex **3** excited at 360 nm.

{(py)$_2$(OMe)COH} of the (py)$_2$CO ligand. The analogous di-nuclear derivatives, [Ln$_2$(NO$_3$)$_3${(py)$_2$C(OMe)O}$_2${(py)$_2$C(OH)O}] [Ln = Tb and Er], were synthesized from the reaction of (py)$_2$CO with the Er(NO$_3$)$_3$·6H$_2$O salt. The di-nuclear complexes were formed through the coordination action of multiple bridging of the *gem*-diol {(py)$_2$(OH)CO}$^-$ and hemiacetal form [{(py)$_2$(OMe)CO}$^-$] of the (py)$_2$CO ligand.[29] Two types of Er(III) centers were observed: one Er(III) center is nine-coordinated with a distorted tricapped trigonal-prismatic geometry, and the other is eight-coordinated with a distorted dodecahedral geometry. Solid-state luminescence studies at room temperature of the analogous di-nuclear Eu^{III} and Tb^{III} complexes revealed red and green emissions, respectively.[29] Similar types of acetal formation have been reported using single-crystal X-ray crystallography for [Ln(NCS)$_3${(py)$_2$C(OEt)(OH)}$_3$] [Pr(III), Sm(III) and Gd(III)] complexes.[30] One tetrahedrally shaped tetranuclear complex, [Dy$_4$(NO$_3$)(HL)$_4${(py)$_2$C(OH)O}$_2$]·(OH)·6CH$_3$CN·0.5H$_2$O, has been reported that utilized the Schiff base 2-((2-hydroxybenzylidene)amino) propane-1,3-diol ligand (H_3L) and the mono-deprotonated form of the *gem*-diol, [(py)$_2$(OH)CO]$^-$, derived from the (py)$_2$CO ligand.[31] Here {(py)$_2$(OH)CO}$^-$ acts as an auxiliary coordinating ligand. This complex showed slow magnetic relaxation at low temperatures. The non-nuclear derivative [Dy$_9$(μ_3-OH)$_8$(μ_4-OH)$_2$(N$_3$)$_8${(py)$_2$C(OCH$_3$)O}$_8$]·(OH)·(4H$_2$O) has been synthesized by the reaction of (py)$_2$CO, NaN$_3$ and Dy(NO$_3$)$_3$·5H$_2$O. This complex is formed by the hemiacetal {(py)$_2$(OMe)CO}$^-$ and showed slow relaxation of magnetization.[32]

Theoretical studies and magnetic properties

Herein, we carried out *ab initio* calculations to shed light on the magnetic anisotropy and magnetic relaxation pathways in complexes **1–6**. All calculations were carried out using the OpenMOLCAS code.[33] Complete active space self-consistent field (CASSCF) calculations were performed using an active space of CAS(n,7) (where n = 3 (Nd(III)), 6 (Eu(III)), 9 (Dy(III)), 8 (Tb(III)), 11 (Er(III)) and 13 (Yb(III)) ions) to compute the spin-free and spin–orbit states. Next, we mixed these spin-free states using the restricted active space state interaction-spin orbit (RASSI-SO) module and computed the spin–orbit states. Subsequently, we used the SINGLE_ANISO module to extract the relevant spin-Hamiltonian parameters for complexes **1–6**. This methodology has been used widely to compute the electronic and magnetic properties of mononuclear and polynuclear lanthanide complexes.[34,35] To compute the single-ion anisotropy in the complexes, we substituted three Ln(III) ions with a diamagnetic Lu(III) ion and performed CASSCF calculations on the paramagnetic Ln(III) ions. Complexes **1–6** are tetranuclear complexes, where two dimeric [Ln$_2$(μ_3-OH){py$_2$C(OH)O}(O$_2$CCMe$_3$)$_4$] [where Ln = Nd (**1**), Eu (**2**), Tb (**3**), Dy (**4**), Er (**5**) and Yb (**6**)] units are bridged through the μ_3-OH and {py$_2$C(OH)O}$^-$ ligands. In complexes **1–6**, there are two types of eight-coordinated Ln(III) centres: one with an [{LnO$_8$}] coordination environment and the other with an [{LnO$_6$N$_2$}] environment. These adopt distorted elongated trigonal bipyramidal and distorted Johnson elongated triangular bipyramidal geometries, respectively. Here, for clarity, we denoted individual centres as Ln@X (where Ln = Nd, Eu, Tb, Dy, Er, or Yb, and X = 1–4 refers to the centre position within complexes **1–6**). Owing to the presence of inversion symmetry, centres Ln@1 and Ln@3 exhibit the [{LnO$_8$}] core, while centres Ln@2 and Ln@4 feature the [{LnO$_6$N$_2$}] core across all complexes **1–6**.

In the case of complex **1**, the ground state of Nd(III) possesses a $^4I_{9/2}$ term, and here, using an active space of CAS(3,7), we computed all 35 quartets. For the Nd@1/3 and Nd@2/4 centres, the energies of five low-lying Kramers doublets (KDs) span over an energy range of ~363 and ~357 cm^{-1}, with the first excited state at ~82 and ~72 cm^{-1}, respectively. The ground state g-tensors for Nd@1 and Nd@2 centres are g_{xx} = 0.955, g_{yy} = 1.818, g_{zz} = 3.854 and g_{xx} = 3.422, g_{yy} = 2.457, g_{zz} = 0.646, respectively (see Table S12). The wavefunction analysis shows an m_J = |7/2⟩ ground state for Nd@1 and an m_J = |3/2⟩ ground state for Nd@2, along with a strong mixing from other excited states. The g-tensors for the first excited state are g_{xx} = 0.553, g_{yy} = 1.165, g_{zz} = 2.772 for Nd@1 and g_{xx} = 0.645, g_{yy} = 1.245, g_{zz} = 3.316 for Nd@2. Moreover, we observed a large k_{QTM} of 0.46μ_B for Nd@1 and 0.98μ_B for Nd@2 within the ground state KDs, which sets the U_{cal} to be ~82 and ~72 cm^{-1} for Nd@1 and Nd@2, respectively. The Kramers ion with substantial k_{QTM} at ground state KDs speeds up the magnetic relaxation and reduces the SMM behaviour in complex **1**. Next, we computed the crystal field (CF) using the following equation, $H_{CF} = \sum_{k=2,4,6}\sum_{q=-k}^{q=+k} B_k^q \hat{O}_k^q$, where, $\hat{O}_k^q$ represents the extended Stevens operator and B_k^q is the crystal field parameter. The crystal field parameters (B_k^q) for all four individual Nd(III) centers of complex **1** are reported in Table S13. In all four cases, we observed computed axial B_k^q (k = 0, q = 0) and nonaxial B_k^q ($k \neq 0$, q = 2, 4) parameters are competing with each other, which indicates that the crystal field generated by ligands is not completely axial in nature. This is also reflected in the computed transverse components of g-values, which are very large, leading to the large k_{QTM} value. Our spin-Hamiltonian (SH) analysis indicates a very fast QTM within the ground state, which reduces any slow relaxation at the single-ion level.

Complex **2** possesses Eu(III) ions with the [Xe] 4f^6 electronic configuration, while the spin–orbit coupling stabilizes an isotropic $^7F_0$ term as the ground state. Using an active space of CAS(6,7), we computed 7 septets and 140 quintets, and the computed spin-free septet states span an energy window of ~636.0 (642.9) cm^{-1}, for Eu@1/3 (Eu@2/4), respectively, while the quintet states span an energy range of 90620.2 (90709.3) cm^{-1} for Eu@1/3 (Eu@2/4), respectively. Using RASSI-SO, we computed the first excited KDs emerging from the $^7F_1$ term located at 274.7 cm^{-1} and 258.2 cm^{-1} for the Eu@1/3 and Eu@2/4, respectively, with m_J = 0 as the ground state for Eu(III) (Table S14). The computed χT reveals weak temperature-independent paramagnetic behaviour (see Fig. 11).

In complex **4**, the eight low-lying Kramers doublets (KDs) derived from the $^6H_{15/2}$ state span an energy range of 481.3

and 383.1 cm^{-1}, with the first excited KDs located at ~133 and 36 cm^{-1} for the Dy@1/3 and Dy@2/4, respectively. For the Dy@1/3 centres, the computed *g*-values are g_{xx} = 0.087, g_{yy} = 0.201, g_{zz} = 19.477 whereas, for Dy@2/4, the *g*-values are g_{xx} = 0.090, g_{yy} = 0.474, g_{zz} = 17.333. While both centres exhibit axial anisotropy, the Dy@2/4 centres lack the Ising-type feature (g_{zz} ~ 20), as observed in Dy@1/3 (see Table S15). Wavefunction decomposition analysis shows stabilization of pure $m_J|\pm15/2\rangle$ for Dy@1/3, while a mixed ground state composition of 64% $|\pm15/2\rangle$ and 28% $|\pm11/2\rangle$ was observed for the Dy@2/4 centres. The first excited KDs, mainly $|\pm11/2\rangle$, located at ~36 cm^{-1}, strongly mixes with the ground state KDs, resulting in the mixed ground state configuration and decreased axiality in the ground state *g*-values for the Dy@2/4 centres. The computed central magnetic axis (g_{zz}) for the Dy@1/3 centres is aligned towards the O atom of the ligand (~5.2°) and perpendicular to the plane formed for the five O donor atoms (see Fig. 9a, 10a). On the other hand, the ground state g_{zz} axis is aligned towards the μ_3-OH ligand, possessing the largest negative Loprop charges (~23°) (see Fig. 9b). Due to the non-superposition of the orientation of the ground and first excited KDs, it suggests that the magnetic relaxation is likely to occur *via* the first excited KDs, resulting in U_{cal} values of ~133 and 36 cm^{-1} for the Dy@1/3 and Dy@2/4 centres, respectively (see Fig. S13). In addition, due to the sizable transverse magnetic moment (7.2 × $10^{-2}\mu_B$ for Dy@1/3 and 9.4 × $10^{-2}\mu_B$ for Dy@2/4) within the ground state KDs, the quantum tunnelling of magnetization (QTM) is likely to be a competing mechanism for magnetic relaxation. This discrepancy in the *g*-values and computed U_{cal} values for both centres is attributed to the differences in the local structural environment, and is reflected in the computed crystal field parameters. For both the centers, we observed that the non-axial B_k^q terms ($q \neq 0$ and k = 2, 4) are dominant and compete with the axial (q = 0 and k = 2, 4) terms (see Table S16), which clearly reflects that the ligand field around both the Ln(III) centres is not completely axially anisotropic in nature. Second, the computed axial crystal field parameters are −1.58 for Dy@1/3 centres and −7.06 × 10^{-1} for Dy@2/4 centres. Thus, Dy@2/4 centres are ~10× weaker, highlighting why the first excited KDs are much lower in energy for the Dy@2/4 centres.

For complex **3**, the low-lying pseudo-doublets derived from the ground $^7F_6$ multiplets span ~499 (352) cm^{-1} with the first excited state at 118.7 (63.9) cm^{-1} for Tb@1/3 (Tb@2/4) centres. Due to the similarity in the local structural parameters, the splitting pattern for Tb(III) centres are two distinct Dy centers in complex **4**. Wavefunction decomposition analysis predicts a pure 98% $|\pm6\rangle$ for Tb@1/3 centres and a mixed m_J state 84% $|\pm6\rangle$ + 12% $|\pm4\rangle$ as the ground state for Tb@2/4 centres. The computed ground state *g*-values are highly axial, with g_{zz} ~ 17.797 (17.049) and with substantial ground state tunnel splitting of 0.2 (0.7) cm^{-1} for Tb@1/3 (Tb@2/4) centres (see Table S17). Based on CASSCF computations, the main magnetic axes of the ground state are oriented towards the –O atom (30°) of the ligand for Tb@1/3 and the N atom (33°) of the ligand for Tb@2/4 (see Fig. 9, 10b), which is similar to what was observed for the Dy(III) centres in complex **4**. The computed U_{cal} values are ~118.7 (63.9) cm^{-1} for Tb@1/3 (Tb@2/4) with large ground state tunnel splitting. Due to large tunnel splitting in non-Kramer ions, the QTM is likely to be the dominant mechanism of magnetic relaxation in complex **3**. The computed CF parameters show significant non-axial terms, indicating that the local ligand field around the Tb@1/3 and Tb@2/4 centres is non-axial, resulting in the giant QTM within the ground state pseudo-KDs (see Table S18).

In complex **5**, we computed all 35 quartets using an active space of CAS(11,7). The calculated spectrum of the spin-free quartet states spanned an energy window of ~46977.7 (46961.0) cm^{-1} for Er@1/3 (Er@2/4), respectively. RASSI-SO computations revealed that the energy spectrum of eight low-

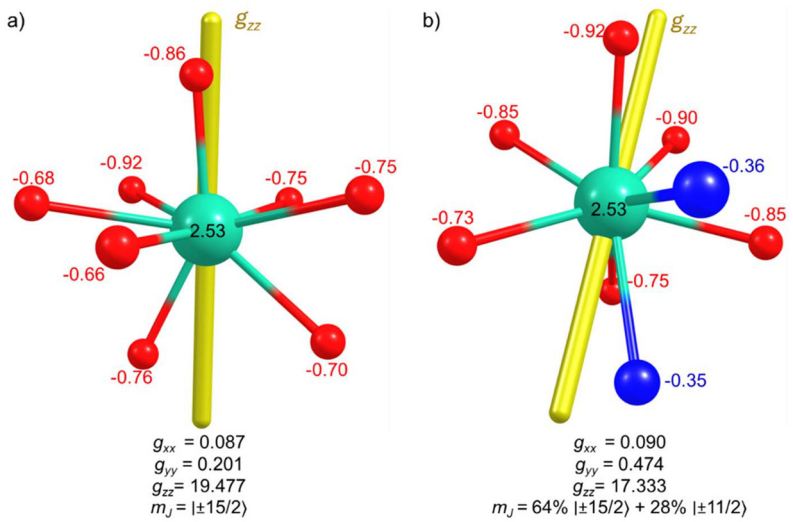

Fig. 9 CASSCF-computed LoProp charges on the Dy@1 (a) and Dy@2 (b) first coordination sphere ligated atoms, along with the orientation of the main magnetic axis g_{zz} in complex **4**.

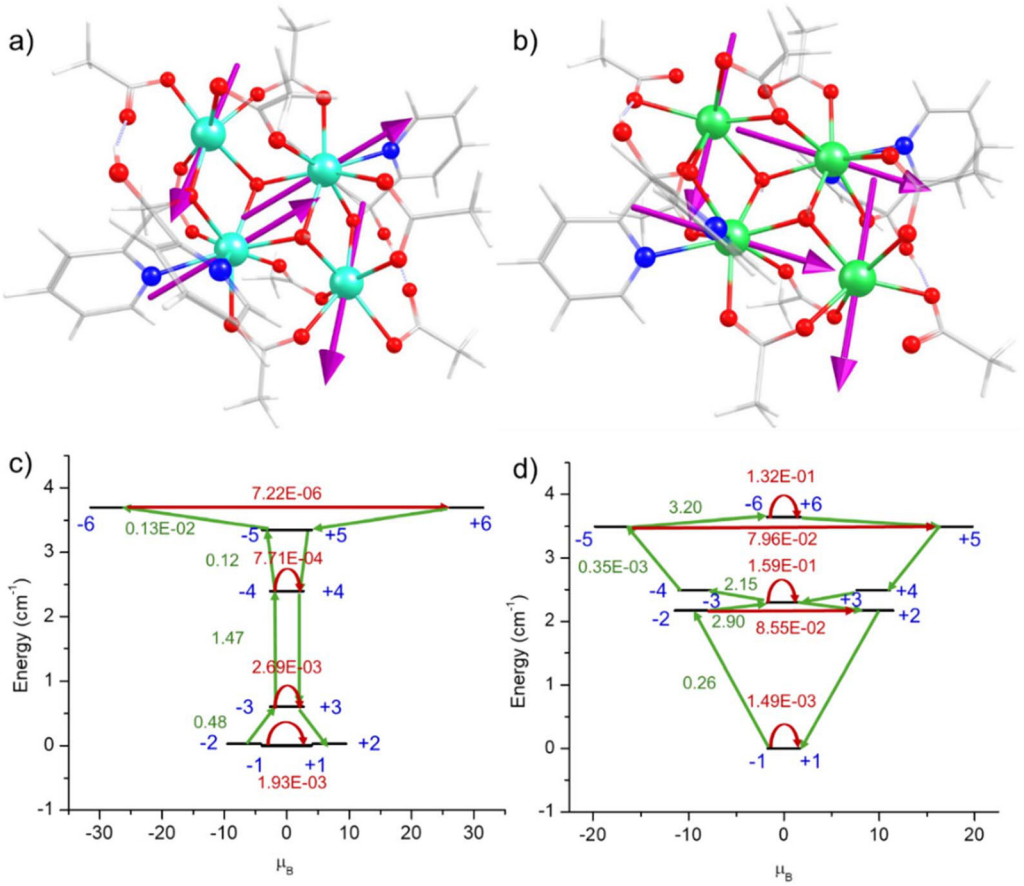

Fig. 10 SINGLE_ANISO-computed orientation of the ground state main magnetic axis (g_{zz}) of the individual centres in (a) complex **4**, and (b) complex **3**. POLY_ANISO-computed *ab initio* blockade barrier for (c) complex **4** and (d) complex **3**. [Color code: teal (Dy), green (Tb), red (O), blue (N), grey (C), white (H)].

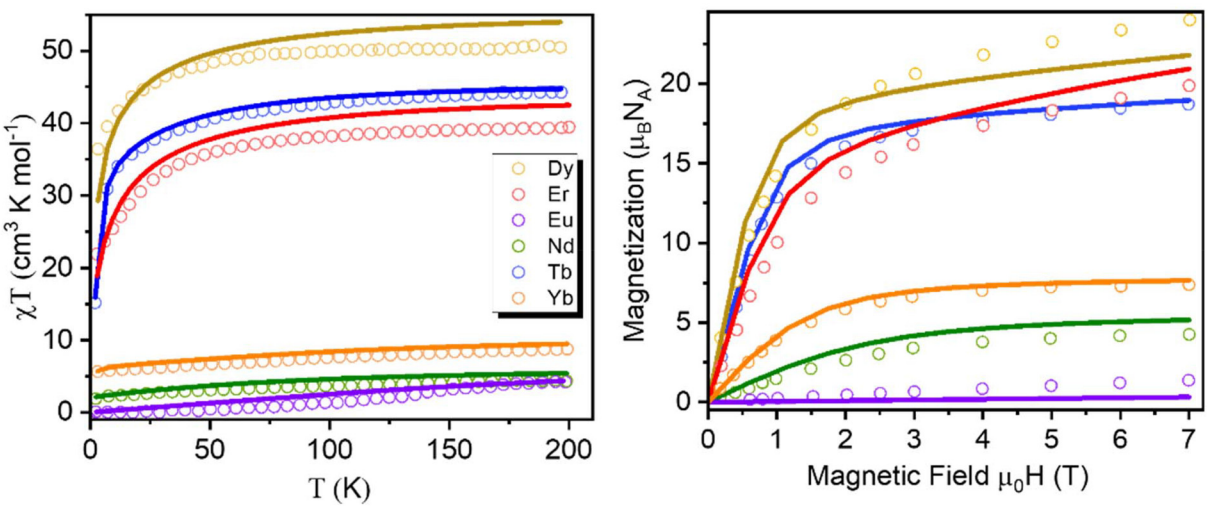

Fig. 11 (Left) Thermal dependence of the molecular magnetic susceptibility for Ln_4 complexes. The simulated results are scaled up by 3% in order to make it compatible with experimental data. (Right) Magnetization (*M*) *versus* magnetic field (*H*) plot for all the complexes at 2 K. The circles indicate the experimental values, while the lines represent the POLY_ANISO-simulated data.

lying Kramers doublets (KDs) derived from the $^4I_{15/2}$ state spans an energy range of 304 and 318 cm^{-1}, with the first excited KDs located at ~29 and 22 cm^{-1} for the Er@1/3 and Er@2/4 centres, respectively. For the Er@1/3 centres, the computed *g*-values are g_{xx} = 2.348, g_{yy} = 2.782, g_{zz} = 12.600 whereas, for the Er@2/4 centres, *g*-values are g_{xx} = 0.951, g_{yy} = 2.035, g_{zz} = 14.646 (see Table S23) (Table S23). While both centres exhibit axial anisotropy, they lack the Ising-type feature (g_{zz} ~ 20), as they possess a significant transverse component. Wavefunction decomposition analysis shows stabilisation of pure m_J $|\pm 15/2\rangle$ as the ground state for both Er(III) centres. The first excited KDs have *g*-values of g_{xx} = 7.267, g_{yy} = 5.607, g_{zz} = 2.324, and g_{xx} = 0.183, g_{yy} = 2.639, g_{zz} = 12.654 for Er@1 and Er@2, respectively. Similar to complex **1**, a large k_{QTM} (0.86μ_B for Er@1 and 0.50μ_B for Er@2) is observed for Er(III) centres, which suggests dominance of the QTM in the ground state. This is further supported by the computed CF parameters (see Table S24), where non-axial terms are significantly larger than the axial terms. In complex **6**, the ground state of Yb(III) possesses a $^2F_{7/2}$ term, and here, using an active space of CAS (13,7), we computed all 7 septets. The four Kramers doublets generated from the $^2F_{7/2}$ state span up to 376.9 cm^{-1} and 460.7 cm^{-1} for Yb@1/3 and Yb@2/4, respectively. For the Yb@1/3 centres, the computed *g*-values are g_{xx} = 1.434, g_{yy} = 1.908, g_{zz} = 6.308, whereas, for Yb@2/4, the *g*-values are g_{xx} = 0.615, g_{yy} = 1.122, g_{zz} = 7.323 with large k_{QTM} of 0.56μ_B for Yb@1 and 0.29μ_B for Yb@2 for the ground state KDs (see Table S25). The strong transverse anisotropy results in the large k_{QTM} value within the ground-state-connecting doublet, which indicates the presence of strong ground-state QTM. The computed CF parameters show large and sizable non-axial terms, which compete with the axial term, highlighting that a mixed crystal field significantly enables the ground state QTM (see Table S26).

Next, we extracted the magnetic exchange interaction between the Ln(III) centres in all complexes by fitting the experimental static DC magnetic susceptibility and magnetization data (Fig. 11). Here, we used the $\hat{H} = -\hat{J}(S_1 \cdot S_2)$ formalism using the POLY_ANISO code, where *J* is the magnetic exchange interaction that contains both the exchange ($\hat{J}_{ex}$) and dipolar coupling ($\hat{J}_{dipo}$), while S_1 and S_2 represent the projections of the pseudo-spin $S = \frac{1}{2}$ of the ground state. The simulation nicely reproduces the experimental magnetic susceptibility data for complexes **1–6** (see Fig. 11). All the complexes possess butterfly cores where two Ln(III) centres are in the body position while the other two Ln(III) centres are in the wing position, leading to three distinct magnetic exchange couplings (J_1–J_3) (see Fig. S14 in the SI). The best fits of experimental magnetic susceptibility (J_{total}) along with magnetic exchange values (J_{ex}) for complexes **1–6** are reported in Table 1.

The best fits of experimental magnetic susceptibility yield J_{total} values of −0.10 (J_1), −0.14 (J_2), −0.06 (J_3) cm^{-1} for complex **4** while J_{total} values of −0.12 (J_1), −0.14 (J_2), −0.07 (J_3) cm^{-1} were obtained for complex **3** with a small intermolecular interaction z_J of −0.002 cm^{-1} for both complexes (see Tables S19 and S21).[34d] Additionally, we determined the contributions

Table 1 Exchange and dipolar interactions were obtained from the POLY_ANISO simulations from the best fit using the Lines model for complexes **1–6** with z_J = −0.002

	1			**2**			**3**			**4**			**5**			**6**		
	J_1	J_2	J_3	J_1	J_2	J_3	J_1	J_2	J_3	J_1	J_2	J_3	J_1	J_2	J_3	J_1	J_2	J_3
J_{tot}	−0.06	−0.09	−0.04	−0.09	−0.07	−0.03	−0.10	−0.14	−0.06	−0.12	−0.14	−0.07	−0.15	−0.14	−0.09	−0.09	−0.08	−0.04
J_{ex}	−0.04	−0.07	−0.03	−0.08	−0.06	−0.02	−0.09	−0.12	−0.05	−0.07	−0.09	−0.06	−0.12	−0.11	−0.10	−0.07	−0.06	−0.03
J_{dipo}	−0.02	−0.02	−0.01	−0.01	−0.01	−0.01	−0.01	−0.02	−0.01	−0.05	−0.05	−0.01	−0.03	−0.03	0.01	−0.02	−0.02	−0.01

of J_{ex}/J_{dipo} to the J_{tot} values by turning off the dipolar interactions, and the best-fits yield J_{ex}/J_{dipo} values of −0.09/−0.01, −0.12/−0.02, −0.05/−0.01 for complex **4** and −0.07/−0.05, −0.09/−0.05, −0.06/−0.01 cm^{-1} for complex **3**. It is evident from the fitting that both the exchange and dipolar interactions are antiferromagnetic in nature for both the complexes. Moreover, the exchange contributions (arising through bonds and space) are dominated significantly by dipolar interactions. Next, we constructed the exchange spectrum of complexes **4** and **3**, where a non-Kramers-type exchange-coupled ground state is observed for both complexes (Fig. 10c and d). In both complexes, the exchange-coupled ground state shows g_{zz} values of ~2.6654 (**4**) and 0.0021 (**3**), resulting from the antiferromagnetic interaction between the Ln(III) centers (see Tables S20 and S22). For both complexes **4** and **3**, we observed a sizable tunnel splitting of 1.9×10^{-3} cm^{-1} and 1.5×10^{-3} cm^{-1}, indicating that QTM is still a dominant mechanism for magnetic relaxation in the exchange-coupled systems, resulting in diminishing SMM behaviour. Despite having a strong antiferromagnetic coupling between the Ln(III) centres, a distorted local geometry around the Ln(III) centre fails to isolate a large m_J as the ground state, which in turn diminishes the SMM behaviour for both complexes **3** and **4**.

In order to check experimentally whether these complexes exhibit slow spin–lattice relaxation processes, AC susceptibility was measured at 2 K from 50 Hz to 10 kHz, as shown in Fig. S15 in the SI. To suppress quantum tunnelling as a potential relaxation process of magnetic reversal, the AC susceptibility was not only measured at zero DC magnetic field, but also at various DC fields (up to about 2500 Oe for selected complexes). None of the complexes **1** (Nd), **3** (Tb), **4** (Dy), **5** (Er), and **6** (Yb) exhibited AC susceptibility data that would clearly indicate the existence of slow magnetic relaxation with a clear maximum of the imaginary χ'' signal within the available experimental parameter space. Only complex **3** (Tb) shows an increase of the χ'' signal close to the maximum frequency of 10 kHz that might indicate the presence of slow relaxation at even higher frequencies. For complex **2** (Eu), AC susceptibility could not be measured due to its weak magnetic signal at low temperature.

Conclusion

We utilized the di-2-pyridyl ketone ligand for the first time to assemble homometallic tetranuclear Ln^{III}_4 ensembles. The core structure of this family consists of two *O-capped* subunits. The four Ln(III) ions are coplanar and lie in the same plane. Each complex contains two types of eight-coordinated lanthanide centers *viz.* the Ln1 center that possesses a distorted elongated trigonal bipyramidal geometry and the Ln2 center that has a distorted Johnson elongated triangular bipyramidal geometry. All the complexes show strong intramolecular hydrogen bonding within their molecular integrity and the H-bond distances decrease according to the lanthanide contraction of the complex. Photoluminescence studies of these complexes show that the di-2-pyridyl ketone ligand sensitizes compound **3**, but for all other complexes, intense ligand center emission peaks are observed. For compound **3**, intense emission peaks at 493, 548, 586, and 622 nm are observed upon excitation at 360 nm in the solid state at room temperature. CASSCF calculations were performed on complexes **1–6** for magnetic anisotropy, magnetic relaxation pathways and crystal field (CF) splitting. We used the SINGLE_ANISO module to extract the relevant spin-Hamiltonian parameters for all the complexes. The Kramers ion with substantial k_{QTM} at ground state KDs speeds up the magnetic relaxation, and diminishes the SMM behaviour in complex **1**. We computed the crystal field and observed that the axial parameters compete with each other, which indicates that the crystal field generated by the ligands is not completely axial in nature. Complexes **3** and **4** show that the distorted geometry around the Ln(III) centres fails to stabilize the largest m_J as the ground state, which in turn diminishes the SMM behaviour, despite sizable antiferromagnetic interactions between the Ln(III) centres. For complex **4**, due to the non-superposition of the orientation of the ground and first excited KDs, it is suggested that magnetic relaxation is likely to occur *via* the first excited KDs. We have calculated that magnetic exchange interactions indicate three distinct magnetic couplings (J_1–J_3). AC susceptibility measurements of the complexes at 2 K did not exhibit any local maximum of the imaginary χ'' component that would have been characteristic for the realization of slow spin–lattice relaxation, neither at zero DC field nor at various DC fields. However, complex **3** (Tb) shows an increase of the χ'' signal close to the maximum frequency of 10 kHz that might indicate the presence of slow relaxation at even higher frequencies. We are currently exploring di-2-pyridyl ketone ligand-based lanthanide complexes by changing the reaction conditions to afford lanthanide clusters featuring different coordination numbers and geometries. These manuscripts are in preparation.

Conflicts of interest

There is no conflict of interest.

Data availability

All the data are available in the main manuscript or in the SI: Figures and tabulated bond angles/lengths for all compounds. IR, photoluminescent spectra, *Ac* susceptibility measurements. Single-crystal data[18a–f] and the CIFs have been deposited with the CCDC for complexes **1–6**. CCDC 2379210–2379215 contain the supplementary crystallographic data for this paper.[36a–f] Full results of the SHAPE analysis for the Ln(III) centers in **1–6** using SHAPE 2.1.[22] All these theoretical calculations were carried out using the OpenMOLCAS code.[33] See DOI: **https://doi.org/10.1039/d4dt02976c**.

Acknowledgements

We thank the Department of Science and Engineering Research Board (SERB), India, for financial support through the Ramanujan fellowship (SERB/F/10742/202-2022). J. G. thanks the Department of Chemistry, Jadavpur University, the University of Delhi, and the Institution of Eminence (IoE) for the FRP research Grant (Ref. No./IoE/2023-24/12/FRP). S. K. S. acknowledges the Science and Engineering Research Board (SERB) for the Core Research Grant (CRG/2023/002936) and IIT Hyderabad for its generous funding. I. T. thanks UGC for the NFOBC fellowship.

References

1 (*a*) D. N. Woodruff, R. E. P. Winpenny and R. A. Layfield, Lanthanide single-molecule magnets, *Chem. Rev.*, 2013, **113**, 5110–5148, DOI: 10.1021/cr400018q; (*b*) J. Goura and V. Chandrasekhar, Molecular Metal Phosphonates, *Chem. Rev.*, 2015, **115**, 6854–6965, DOI: 10.1021/acs.chemrev.5b00107; (*c*) S.-R. Li, W.-D. Liu, L.-S. Long, L.-S. Zheng and X.-J. Kong, Recent advances in polyoxometalate-based lanthanide–oxo clusters, *Polyoxometalates*, 2023, **2**, 9140022, DOI: 10.26599/POM.2023.9140022.

2 (*a*) T. C. Stamatatos, C. G. Efthymiou, C. C. Stoumpos and S. P. Perlepes, Adventures in the Coordination Chemistry of Di-2-pyridyl Ketone and Related Ligands: From High-Spin Molecules and Single-Molecule Magnets to Coordination Polymers, and from Structural Aesthetics to an Exciting New Reactivity Chemistry of Coordinated Ligands, *Eur. J. Inorg. Chem.*, 2009, 3361–3391, DOI: 10.1002/ejic.200900223; (*b*) G. S. Papaefstathiou and S. P. Perlepes, Families of Polynuclear Manganese, Cobalt, Nickel and Copper Complexes Stabilized by Various Forms of Di-2-pyridyl Ketone, *Comments Inorg. Chem.*, 2002, **23**, 249–274, DOI: 10.1080/02603590213135.

3 H. Mori, K. Sakamoto, Y. Masudo, Y. Matsuoka, M. Matsubayashi and K. Sakai, Aerial Oxidation of Some 2-Pyridyl Ketone Hydrazones Catalyzed by Cu^{2+}. Physical Properties of Reaction Products, *Chem. Pharm. Bull.*, 1993, **41**, 1944–1947, DOI: 10.1248/cpb.41.1944.

4 M. Shiddiq, D. Komijani, Y. Duan, A. Gaita-Ariño, E. Coronado and S. Hill, Enhancing coherence in molecular spin qubits via atomic clock transitions, *Nature*, 2016, **531**, 348–351, DOI: 10.1038/nature16984.

5 L. Bogani and W. Wernsdorfer, Molecular spintronics using single-molecule magnets, *Nat. Mater.*, 2008, **7**, 179–186, DOI: 10.1038/nmat2133.

6 (*a*) M. Mannini, F. Pineider, P. Sainctavit, C. Danieli, E. Otero, C. Sciancalepore, A. M. Talarico, M. A. Arrio, A. Cornia, D. Gatteschi and R. Sessoli, Magnetic memory of a single-molecule quantum magnet wired to a gold surface, *Nat. Mater.*, 2009, **8**, 194–197, DOI: 10.1038/nmat2374; (*b*) S. Thiele, F. Balestro, R. Ballou, S. Klyatskaya, M. Ruben and W. Wernsdorfer, Electrically driven nuclear spin resonance in single-molecule magnets, *Science*, 2014, **344**, 1135–1138, DOI: 10.1126/science.1249802.

7 Y. Z. Zheng, G. J. Zhou, Z. Zheng and R. E. P. Winpenny, Molecule-based magnetic coolers, *Chem. Soc. Rev.*, 2014, **43**, 1462–1475, DOI: 10.1039/C3CS60337G.

8 Y.-J. Ma, J.-X. Hu, S.-D. Han, J. Pan, J.-H. Li and G.-M. Wang, Manipulating On/Off Single-Molecule Magnet Behavior in a Dy(III)-Based Photochromic Complex, *J. Am. Chem. Soc.*, 2020, **142**, 2682–2689, DOI: 10.1021/jacs.9b13461.

9 J. D. Rinehart and J. R. Long, Exploiting single-ion anisotropy in the design of f-element single-molecule magnets, *Chem. Sci.*, 2011, **2**, 2078–2085, DOI: 10.1039/C1SC00513H.

10 H. Schilder and H. Lueken, Computerized magnetic studies on d, f, d–d, f–f, and d–S, f–S systems under varying ligand and magnetic fields, *J. Magn. Magn. Mater.*, 2004, **281**, 17–26, DOI: 10.1016/j.jmmm.2004.03.041.

11 N. Ishikawa, Simultaneous Determination of Ligand-Field Parameters of Isostructural Lanthanide Complexes by Multidimensional Optimization, *J. Phys. Chem. A*, 2003, **107**, 5831–5835, DOI: 10.1021/jp034433a.

12 T. Han, Y.-S. Ding, J.-D. Leng, Z. Zheng and Y.-Z. Zheng, Polymeric Perturbation to the Magnetic Relaxations of the C_{2v} - Symmetric $[Er(Cp)_2(OBu)_2]^-$ Anion, *Inorg. Chem.*, 2015, **54**, 4588–4590.

13 G. Novitchi, S. Jiang, S. Shova, F. Rida, I. Hlavička, M. Orlita, W. Wernsdorfer, R. Hamze, C. Martins, N. Suaud, N. Guihéry, A.-L. Barra and C. Train, From Positive to Negative Zero-Field Splitting in a Series of Strongly Magnetically Anisotropic Mononuclear Metal Complexes, *Inorg. Chem.*, 2017, **56**(24), 14809–14822, DOI: 10.1021/acs.inorgchem.7b01861.

14 (*a*) V. Vieru, S. Gómez-Coca, E. Ruiz and L. F. Chibotaru, Increasing the Magnetic Blocking Temperature of Single-Molecule-Magnets, *Angew. Chem.*, 2024, **136**, e202303146, DOI: 10.1002/anie.202303146; (*b*) F.-S. Guo, B. M. Day, Y.-C. Chen, M.-L. Tong, A. Mansikkamäki and R. A. Layfield, Magnetic hysteresis up to 80 kelvin in a dysprosium metallocene single-molecule magnet, *Science*, 2018, **362**, 1400–1403, DOI: 10.1126/science.aav0652.

15 (*a*) T. Pugh, N. F. Chilton and R. A. Layfield, A Low-Symmetry Dysprosium Metallocene Single-Molecule Magnet with a High Anisotropy Barrier, *Angew. Chem., Int. Ed.*, 2016, **55**, 11082–11085, DOI: 10.1002/anie.201604346; (*b*) J. C. Vanjak, B. O. Wilkins, V. Vieru, N. S. Bhuvanesh, J. H. Reibenspies, C. D. Martin, L. F. Chibotaru and M. Nippe, A High-Performance Single-Molecule Magnet Utilizing Dianionic Aminoborolide Ligands, *J. Am. Chem. Soc.*, 2022, **144**, 17743–17747, DOI: 10.1021/jacs.2c06698; (*c*) J. Tang and P. Zhang, *Lanthanide single molecule magnets*, Springer, Berlin Heidelberg, 2015.

16 (*a*) S. Mondal, D. Chauhan, T. Guizouarn, F. Pointillart, G. Rajaraman, A. Steiner and V. Baskar, Self-Assembled Lanthanide Phosphinate Square Grids (Ln = Er, Dy, and Tb): Dy_4 Shows SMM/SMT and Tb_4 SMT Behavior, *Inorg.*

Chem., 2024, **63**, 22338–22348, DOI: **10.1021/acs.inorgchem.4c02567**; (*b*) P. Kumar, A. Swain, J. Acharya, Y. Li, V. Kumar, G. Rajaraman, E. Colacio and V. Chandrasekhar, Synthesis, Structure, and Zero-Field SMM Behavior of Homometallic Dy_2, Dy_4, and Dy_6 Complexes, *Inorg. Chem.*, 2022, **61**, 11600–11621, DOI: **10.1021/acs.inorgchem.2c01041**; (*c*) J. Goura, J. P. S. Walsh, F. Tuna and V. Chandrasekhar, Tetranuclear Lanthanide(III) Complexes in a Seesaw Geometry: Synthesis, Structure, and Magnetism, *Inorg. Chem.*, 2014, **53**, 3385–3391, DOI: **10.1021/ic4027915**.

17 B. S. Furniss, A. J. Hannaford, P. W. G. Smith and A. R. Tatchell, *Vogel's Textbook of Practical Organic Chemistry*, 5th edn, Longman, London, 1989.

18 (*a*) *SMART & SAINT Software Reference manuals, Version 6.45*, Bruker Analytical X-ray Systems, Inc., Madison, WI, 2003; (*b*) G. M. Sheldrick, *SADABS, a software for empirical absorption correction, Ver. 2.05*, University of Göttingen, Göttingen, Germany, 2002; (*c*) *SHELXTL Reference Manual, Ver. 6.c1*, Bruker Analytical X-ray Systems, Inc., Madison, WI, 2000; (*d*) G. M. Sheldrick, *SHELXTL, Ver. 6.12*, Bruker AXS Inc., Madison, WI, 2001; (*e*) G. M. Sheldrick, *SHELXL97, Program for Crystal Structure Refinement*, University of Göttingen, Göttingen, Germany, 1997; (*f*) K. Bradenburg, *Diamond, Ver. 3.1eM*, Crystal Impact GbR, Bonn, Germany, 2005.

19 (*a*) A. J. Tasiopoulos and S. P. Perlepes, Diol-type ligands as central 'players' in the chemistry of high-spin molecules and single-molecule magnets, *Dalton Trans.*, 2008, 5537–5555, DOI: **10.1039/b805014g**; (*b*) C. G. Efthymiou, C. P. Raptopoulou, A. N. Georgopoulou, A. Escuer, C. Papatriantafyllopoulou and S. P. Perlepes, Initial employment of di-2-pyridyl ketone as a route to nickel(II)/lanthanide(III) clusters: triangular Ni_2Ln complexes, *Dalton Trans.*, 2010, **39**, 8603–8605, DOI: **10.1039/c0dt00493f**; (*c*) C. G. Efthymiou, T. C. Stamatatos, C. Papatriantafyllopoulou, A. J. Tasiopoulos, W. Wernsdorfer, S. P. Perlepes and G. Christou, Nickel/Lanthanide Single-Molecule Magnets: {Ni_3Ln} "Stars" with a Ligand Derived from the Metal-Promoted Reduction of Di-2-pyridyl Ketone under Solvo thermal Conditions, *Inorg. Chem.*, 2010, **49**, 9737–9739, DOI: **10.1021/ic101504c**; (*d*) A. N. Georgopoulou, C. G. Efthymiou, C. Papatriantafyllopoulou, V. Psycharis, C. P. Raptopoulou, M. Manos, A. J. Tasiopoulos, A. Escuer and S. P. Perlepes, Triangular $NiII_2LnIII$ and $NiII_2YIII$ complexes derived from di-2-pyridyl ketone: Synthesis, structures and magnetic properties, *Polyhedron*, 2011, **30**, 2978–2986, DOI: **10.1016/j.poly.2011.02.010**; (*e*) M. Savva, K. Skordi, A. D. Fournet, A. E. Thuijs, G. Christou, S. P. Perlepes, C. Papatriantafyllopoulou and A. J. Tasiopoulos, Heterometallic $MnIII_4Ln_2$ (Ln = Dy, Gd, Tb) Cross-Shaped Clusters and Their Homometallic $MnIII_2MnII_2$ Analogues, *Inorg. Chem.*, 2017, **56**, 5657–5668, DOI: **10.1021/acs.inorgchem.7b00191**; (*f*) M. Savva, D. I. Alexandropoulos, M. Pissas, S. P. Perlepes, C. Papatriantafyllopoulou, Y. Sanakis and A. J. Tasiopoulos, Heterometallic clusters based on an uncommon asymmetric "V-shaped" [Fe^{3+}(μ-OR)Ln^{3+} (μOR)$_2Fe^{3+}$]$^{6+}$ (Ln = Gd, Tb, Dy, Ho) structural core and the investigation of the slow relaxation of the magnetization behaviour of the [Fe_2Dy] analogue, *Dalton Trans.*, 2023, **52**, 6997–7008, DOI: **10.1039/d2dt03938a**.

20 R. Jagannathan and S. Soundararajan, Complexes of rare earth perchlorates with di-2-pyridyl ketone, *J. Inorg. Nucl. Chem.*, 1980, **42**, 145–147, DOI: **10.1016/0022-1902(80)80066-2**.

21 (*a*) R. O. Day, J. M. Holmes, V. Chandrasekhar and R. R. Holmes, A new structural form of tin in an oxygen-capped cluster, *J. Am. Chem. Soc.*, 1987, **109**, 940–941, DOI: **10.1021/ja00237a072**; (*b*) D. Maniaki, E. Pilichos and S. P. Perlepes, Coordination Clusters of 3d-Metals That Behave as Single-Molecule Magnets (SMMs): Synthetic Routes and Strategies, *Front. Chem.*, 2018, **6**, 461, DOI: **10.3389/fchem.2018.00461**; (*c*) A. Das, F. J. Klinke, S. Demeshko, S. Meyer, S. Dechert and F. Meyer, Reversible Solvatomagnetic Effect in Novel Tetranuclear Cubane-Type Ni_4 Complexes and Magnetostructural Correlations for the [Ni_4(μ$_3$-O)$_4$] Core, *Inorg. Chem.*, 2012, **51**, 8141–8149, DOI: **10.1021/ic300535d**; (*d*) J. Wang, M. Feng, M. Nadeem Akhtar and M.-L. Tong, Recent advance in heterometallic nanomagnets based on TM_xLn_{4-x} cubane subunits, *Coord. Chem. Rev.*, 2019, **387**, 129–153, DOI: **10.1016/j.ccr.2019.02.008**; (*e*) J. Goura, R. Guillaume, E. Rivière and V. Chandrasekhar, Hexanuclear, Heterometallic, Ni_3Ln_3 Complexes Possessing O-Capped Homo- and Heterometallic Structural Subunits: SMM Behavior of the Dysprosium Analogue, *Inorg. Chem.*, 2014, **53**, 7815–7823, DOI: **10.1021/ic403090z**; (*f*) J. Goura, A. Chakraborty, J. P. S. Walsh, F. Tuna and V. Chandrasekhar, Hexanuclear 3d–4f Neutral $CoII_2LnIII_4$ Clusters: Synthesis, Structure, and Magnetism, *Cryst. Growth. Des*, 2015, **15**, 3157–3165, DOI: **10.1021/acs.cgd.5b00588**; (*g*) B.-Q. Ma, D.-S. Zhang, S. Gao, T.-Z. Jin, C.-H. Yan and G.-X. Xu, From Cubane to Supercubane: The Design, Synthesis, and Structure of a Three-Dimensional Open Framework Based on a Ln_4O_4 Cluster, *Angew Chem., Int. Ed.*, 2000, **39**, 3644–3646, DOI: **10.1002/1521-3757**; (*h*) H. Ke, P. Gamez, L. Zhao, G.-F. Xu, S. Xue and J. Tang, Magnetic Properties of Dysprosium Cubanes Dictated by the M–O–M Angles of the [Dy_4(μ$_3$-OH)$_4$] Core, *Inorg. Chem.*, 2010, **49**, 7549–7557, DOI: **10.1021/ic101057e**.

22 S. Alvarez, P. Alemany, D. Casanova, J. Cirera, M. Llunell and D. Avnir, Shape maps and polyhedral interconversion paths in transition metal chemistry, *Coord. Chem. Rev.*, 2005, **249**, 1693–1708, DOI: **10.1016/j.ccr.2005.03.031**.

23 (*a*) J. Goura, E. Colacio, J. M. Herrera, E. A. Suturina, I. Kuprov, Y. Lan, W. Wernsdorfer and V. Chandrasekhar, Heterometallic Zn_3Ln_3 Ensembles Containing (μ_6-CO_3) Ligand and Triangular Disposition of Ln^{3+} ions: Analysis of Single-Molecule Toroic (SMT) and Single-Molecule Magnet (SMM) Behavior, *Chem. – Eur. J.*, 2017, **23**, 16621–16636, DOI: **10.1002/chem.201703842**; (*b*) R. Jia, H.-F. Li, P. Chen, T. Gao, W.-B. Sun, G.-M. Lia and P.-F. Yan, Synthesis, struc-

ture, and tunable white light emission of heteronuclear Zn_2Ln_2 arrays using a zinc complex as ligand, *CrystEngComm*, 2016, **18**, 917–923, DOI: 10.1039/C5CE02228B.

24 E. Cavalli, S. Ruggieri, S. Mizzoni, C. Nardon, M. Bettinelli and F. Piccinelli, NIR-emission from Yb(III)- and Nd(III)-based complexes in the solid state sensitized by a ligand system absorbing in a broad UV and visible spectral window, *Results Chem.*, 2022, **4**, 100388, DOI: 10.1016/j.rechem.2022.100388.

25 (*a*) A. J. Calahorro, D. Fairen-Jiménez, A. Salinas-Castillo, M. E. López-Viseras and A. Rodríguez-Diéguez, Novel 3D lanthanum oxalate metal-organic-framework: Synthetic, structural, luminescence and adsorption properties, *Polyhedron*, 2013, **52**, 315–320, DOI: 10.1016/j.poly.2012.09.018; (*b*) L.-Z. Zhang, W. Gu, B. Li, X. Liu and D.-Z. Liao, $\{[Nd_4(ox)_4(NO_3)_2(OH)_2(H_2O)_2]\cdot 5H_2O\}_n$: A Porous 3D Lanthanide-Based Coordination Polymer with a Special Luminescent Property, *Inorg. Chem.*, 2007, **46**, 622–624, DOI: 10.1021/ic061635n.

26 (*a*) J. Goura, J. P. S. Walsh, F. Tuna, R. Halder, T. K. Maji and V. Chandrasekhar, P–C Bond Cleavage-Assisted Lanthanide Phosphate Coordination Polymers, *Cryst. Growth Des.*, 2015, **15**, 2555–2560, DOI: 10.1021/cg5017005; (*b*) A. R. Ramya, D. Sharma, S. Natarajan and M. L. P. Reddy, Highly Luminescent and Thermally Stable Lanthanide Coordination Polymers Designed from 4-(Dipyridin-2-yl)aminobenzoate: Efficient Energy Transfer from Tb^{3+} to Eu^{3+} in a Mixed Lanthanide Coordination Compound, *Inorg. Chem.*, 2012, **51**, 8818–8826, DOI: 10.1021/ic300654e.

27 (*a*) S. Titos-Padilla, J. Ruiz, J. M. Herrera, E. K. Brechin, W. Wersndorfer, F. Lloret and E. Colacio, Dilution-Triggered SMM Behavior under Zero Field in a Luminescent Zn_2Dy_2 Tetranuclear Complex Incorporating Carbonato-Bridging Ligands Derived from Atmospheric CO_2 Fixation, *Inorg. Chem.*, 2013, **52**, 9620–9626, DOI: 10.1021/ic401378k; (*b*) J. Ruiz, G. Lorusso, M. Evangelisti, E. K. Brechin, S. J. A. Pope and E. Colacio, Closely-Related $ZnII_2LnIII_2$ Complexes (LnIII = Gd, Yb) with Either Magnetic Refrigerant or Luminescent Single-Molecule Magnet Properties, *Inorg. Chem.*, 2014, **53**, 3586–3594, DOI: 10.1021/ic403097s.

28 K. A. Thiakou, V. Nastopoulos, A. Terzis, C. P. Raptopoulou and S. P. Perlepes, Di-2-pyridyl ketone in lanthanide(III) chemistry: Mononuclear and dinuclear erbium(III) complexes, *Polyhedron*, 2006, **25**, 539–549.

29 K. A. Thiakou, V. Bekiari, C. P. Raptopoulou, V. Psycharis, P. Lianos and S. P. Perlepes, Dinuclear lanthanide(III) complexes from the use of di-2-pyridyl ketone: Preparation, structural characterization and spectroscopic studies, *Polyhedron*, 2006, **25**, 2869–2879.

30 S. Dominguez, J. Torres, J. Gonzalez-platas, M. Hummert, H. Schumann and C. Kremer, Thermodynamic stability and crystal structure of lanthanide complexes with di-2-pyridyl ketonek, *J. Coord. Chem.*, 2009, **62**, 108–119.

31 H.-S. Wang, Z. Zhang, Y. Chen, Z. i.-Q. Pan, Z.-B. Hu and C.-L. Yin, Modulation of the directions of the anisotropic axes of DyIII ions through utilizing two kinds of organic ligands or replacing DyIII ions by FeIII ions, *CrystEngComm*, 2019, **21**, 5429–5439.

32 H.-S. Wang, Q.-Q. Long, C.-L. Yin, Z.-W. Xu and Z.-Q. Pan, Syntheses, crystal structures and magnetic properties of sandglass $DyIII_9$and irregular tetrahedron $DyIII_4$ complexes, *Polyhedron*, 2018, **141**, 69–76.

33 Li Manni, *et al.*, The OpenMolcas Web: A Community-Driven Approach to Advancing Computational Chemistry, *J. Chem. Theory Comput.*, 2023, **19**, 6933–6991, DOI: 10.1021/acs.jctc.3c00182.

34 (*a*) I. Tarannum, S. Moorthy and S. K. Singh, Understanding electrostatics and covalency effects in highly anisotropic organometallic sandwich dysprosium complexes $[Dy(C_mR_m)_2]$ (where R = H, SiH_3, CH_3 and m = 4 to 9): a computational perspective, *Dalton Trans.*, 2023, **52**, 15576–15589, DOI: 10.1039/D3DT01646C; (*b*) K. Kumari, S. Moorthy and S. K. Singh, Single-ion magnet behaviour in highly axial lanthanide mononitrides encapsulated in boron nitride nanotubes: a quantum chemical investigation, *Dalton Trans.*, 2025, **54**, 4715–4727, DOI: 10.1039/D4DT03311F; (*c*) P. Kalita, N. Ahmed, S. Moorthy, V. Béreau, A. K. Bar, P. Kumar, P. Nayak, J.-P. Sutter, S. K. Singh and V. Chandrasekhar, Slow magnetic relaxation in a homoaxially phosphine oxide coordinated pentagonal bipyramidal Dy(iii) complex, *Dalton Trans.*, 2023, **52**, 2804–2815, DOI: 10.1039/D2DT03789K; (*d*) S. Saha, I. Tarannum, P. PalRaktim Datta, S. Bala, A. Ghosh, S. K. Singh and R. Mondal, Electrical–Magnetic Properties of Solvent-Induced Di- and Hexanuclear Lanthanide Complexes Based on an Unorthodox N-Rich Ligand, *Cryst. Growth Des.*, 2025, **25**, 624–638, DOI: 10.1021/acs.cgd.4c01378; (*e*) S. Roy, P. Shukla, N. Ahmed, M.-H. Du, I. Tarannum, X.-J. Kong, T. Gupta, S. K. Singh and S. Das, Interplay between anisotropy and magnetic exchange to modulate the magnetic relaxation behaviours of phenoxo bridged Dy_2 dimers with axial β-diketonate co-ligands, *Dalton Trans.*, 2022, **51**, 18187–18202, DOI: 10.1039/D2DT03117E.

35 (*a*) L. F. Chibotaru and L. Ungur, Ab initio calculation of anisotropic magnetic properties of complexes. I. Unique definition of pseudospin Hamiltonians and their derivation, *J. Chem. Phys.*, 2012, **137**, 064112, DOI: 10.1063/1.4739763; (*b*) W. Zhang, A. Muhtadi, N. Iwahara, L. Ungur and L. F. Chibotaru, Magnetic Anisotropy in Divalent Lanthanide Compounds, *Angew. Chem., Int. Ed.*, 2020, **59**, 12720, DOI: 10.1002/anie.202003399; (*c*) M. Li, H. Wu, Z. Xia, L. Ungur, D. Liu, L. F. Chibotaru, H. Ke, S. Chen and S. Gao, An Inconspicuous Six-Coordinate Neutral DyIII Single-Ion Magnet with Remarkable Magnetic Anisotropy and Stability, *Inorg. Chem.*, 2020, **59**(10), 7158–7166, DOI: 10.1021/acs.inorgchem.0c00616.

36 (*a*) CCDC 2379210: Experimental Crystal Structure Determination, 2025, DOI: 10.5517/ccdc.csd.cc2kvrqx;

(*b*) CCDC 2379211: Experimental Crystal Structure Determination, 2025, DOI: **10.5517/ccdc.csd.cc2kvrry**; (*c*) CCDC 2379212: Experimental Crystal Structure Determination, 2025, DOI: **10.5517/ccdc.csd.cc2kvrsz**; (*d*) CCDC 2379213: Experimental Crystal Structure Determination, 2025, DOI: **10.5517/ccdc.csd.cc2kvrt0**; (*e*) CCDC 2379214: Experimental Crystal Structure Determination, 2025, DOI: **10.5517/ccdc.csd.cc2kvrv1**; (*f*) CCDC 2379215: Experimental Crystal Structure Determination, 2025, DOI: **10.5517/ccdc.csd.cc2kvrw2**.